

# Large-Area and Broadband Thermoelectric Infrared Detection in a Carbon Nanotube Black-Body Absorber

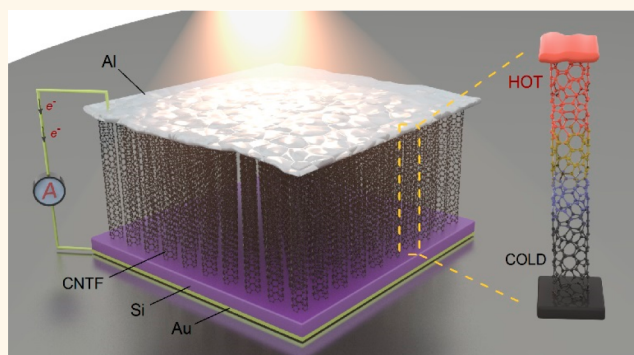
Mingyu Zhang,<sup>†</sup> Dayan Ban,<sup>‡</sup> Chao Xu,<sup>‡</sup> and John T. W. Yeow<sup>\*,†</sup>

<sup>†</sup>Advanced Micro-/Nano-Devices Lab, Department of Systems Design Engineering, University of Waterloo, 200 University Avenue West, Waterloo, Ontario N2L 3G1, Canada

<sup>‡</sup>Waterloo Institute for Nanotechnology and Department of Electrical and Computer Engineering, University of Waterloo, 200 University Avenue West, Waterloo, Ontario N2L 3G1, Canada

## Supporting Information

**ABSTRACT:** Room-temperature mid- and far-infrared photodetectors and energy harvesters meet diverse upcoming demands including health condition monitoring, industrial inspection, and miniaturized power-source for Internet of Things. However, the cryogenic cooling requirement for III–V semiconductors and the inefficient light absorption in two-dimensional (2D) materials, for example, graphene (2.3%) and black phosphorus (~3%), have hindered mid- and far-infrared optoelectronics from widespread applications. Here, we demonstrate a self-powered infrared photodetector as well as energy harvester *via* employing vertical photothermoelectric (PTE) effect of a carbon nanotube forest (CNTF). In the self-assembled anti-reflecting CNTF, 99.4% reflection suppression is observed, resulting in a broadband detectivity of  $1.9 \times 10^7 \text{ cm Hz}^{1/2}$  in 2.5–25  $\mu\text{m}$  spectral range and peak detectivity of  $2.3 \times 10^9 \text{ cm Hz}^{1/2}$  at 4.3 THz *via* nonlithography fabrication. By virtue of vertical architecture, this photodetector exhibits enhanced sensitivity to weak and unfocused infrared illumination, which mitigates the high actuating power density in conventional PTE or field-effect detectors and renders practical infrared detection in the real life.



**KEYWORDS:** mid- and far-infrared, carbon nanotube forest, photothermoelectric, black-body absorption, broadband, self-power

Beyond semiconductor bandgaps, midwave infrared (MWIR, 3–5  $\mu\text{m}$ ), long-wave infrared (LWIR, 8–12  $\mu\text{m}$ ),<sup>1</sup> and far-infrared (15–2000  $\mu\text{m}$  or 0.3–20 THz) absorptions in most solid-state matters are relatively lower compared to visible range. This has been a main obstacle in the development of room-temperature long-wavelength infrared optoelectronics which hold broad interests in biomedical imaging,<sup>2</sup> industrial monitoring, and Internet of Things, *etc.* In particular, the far-infrared or terahertz (THz) inspection is considered a powerful tool that emerges in material characterization, safety inspection, and biological sensing.<sup>3</sup> Strong light–matter interaction in low-dimensional materials have improved detector performance,<sup>4,5</sup> but the percentage of light getting absorbed by two-dimensional (2D) materials is low – up to 2.3% in single-layer graphene<sup>6</sup> and around 3% in black phosphorus.<sup>4</sup> The advent of plasmon resonant structures including grating electrodes<sup>7</sup> and patterned light-active materials<sup>8,9</sup> have largely enhanced light absorption at certain wavelengths. Resonant absorption at 10  $\mu\text{m}$  wavelength

achieved a photoresponsivity of  $0.4 \text{ A W}^{-1}$  in graphene nanoribbons,<sup>10</sup> and the effect of THz plasmon absorption was also demonstrated to enhance detector performance.<sup>11</sup> However, expensive electron-beam lithography (EBL) fabrication prevents these artificial structures from large-area utilization. Meanwhile, quantum-dot-based photodetectors also exhibit growing photosensitivity from visible to mid-infrared range with a merit of low-cost solution processability,<sup>12</sup> but the limitations include high toxicity in heavy-element materials (*i.e.*, mercury cadmium telluride, MCT) and narrow responsive spectra restricted by the finite bandgap and specific particle size. Synthesized by scalable methods (vapor–liquid–solid growth or wet-etching), vertically aligned nanowire arrays made of Si,<sup>13</sup> SiO<sub>2</sub>,<sup>14</sup> ZnO,<sup>15</sup> GaN,<sup>16</sup> GaAs,<sup>17</sup> and InAsSb<sup>18</sup> have been widely reported as anti-reflecting

Received: August 9, 2019

Accepted: November 12, 2019

Published: November 12, 2019

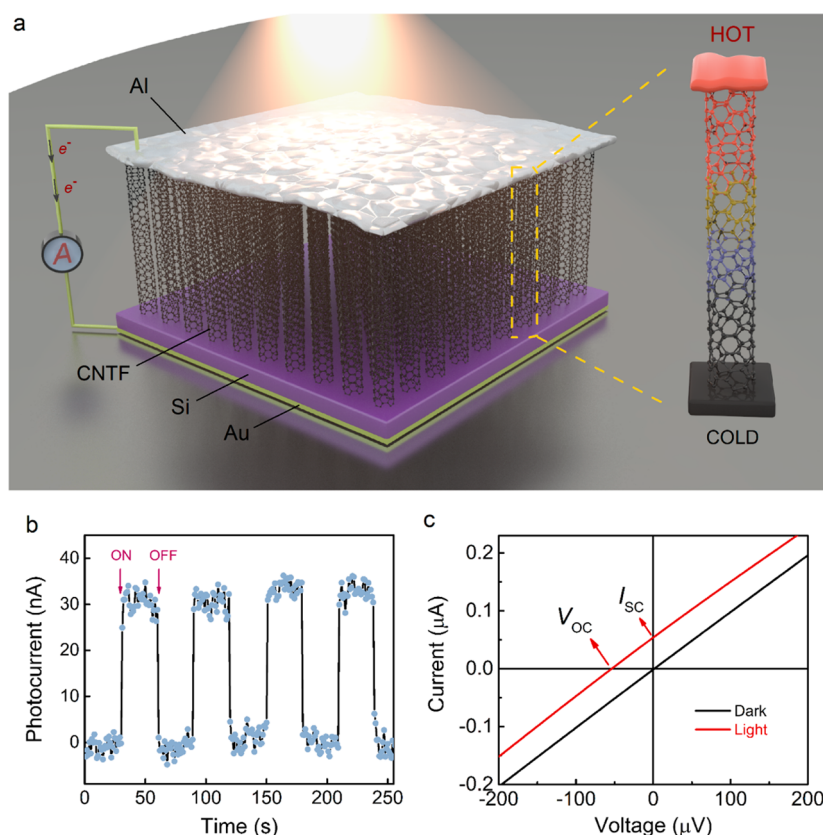


**Figure 1.** CNTF photothermoelectric photodetector. (a) Schematic of the self-powered photodetector. A CNTF covered by top conductive layer (Al) is mounted on a doped-Si substrate with Au back metallization. On the right, the single CNT with top and bottom electrodes illustrates the device temperature gradient induced by infrared illumination. On the left, the black arrows indicate the electrons moving direction due to the thermoelectric effect. (b) Temporal response of the current in a zero-biased device when the black-body illumination is switched on and off periodically. The sampling rate is 1 s. (c) Current–voltage characteristics in the dark and under illumination conditions.  $V_{OC}$  and  $I_{SC}$  are the open-circuit voltage and short-circuit current, respectively. The top-electrode thickness and photosensitive area for the device shown in (b, c) are 25 nm and 1 mm<sup>2</sup>, respectively.

absorbers in the visible and infrared range. As a representative, carbon nanotube forest (CNTF), a self-aligned, densely packed three-dimensional (3D) architecture of carbon nanotubes (CNTs), is renowned for near unity absorption in an ultrabroad infrared range beyond far-infrared.<sup>19–21</sup>

One technical issue for infrared photodetectors using narrow- or zero-bandgap materials such as CNTs, graphene, and MCT is the pronounced dark-current and low signal-to-noise ratio under DC biases at room temperature. This issue has been mitigated by recent studies on room-temperature photothermoelectric (PTE) photodetectors, which exemplify that photons induced thermoelectric effect at zero-bias can reduce the dark current effectively by suppressing  $1/f$  noise and shot noise in circuits.<sup>22–26</sup> At the same time, the PTE effect also sees an improvement with the utilization of low-dimensional materials, benefiting from the enhanced thermoelectric effect due to strong electron density-of-states dependence on energy levels  $dg(E)/dE$ .<sup>27</sup> Walia *et al.* discovered efficient photothermal conversion in vertical GaAs nanowires arrays under external light illumination and revealed a thermal gradient along the nanowires.<sup>17</sup> The demonstration of mid-infrared and THz imaging with PTE photodetectors was achieved by Suzuki *et al.* with a noise equivalent power  $<1$  nW Hz<sup>-1/2</sup> at the CNT/metal interface under ambient conditions.<sup>24</sup>

To date, state-of-the-art mid- and far-infrared photodetectors are still hampered by several challenges: (1) High infrared reflection in low-dimensional materials due to high conductivities along zigzag directions of 2D sheets and along axis direction of one-dimensional (1D) nanowires; (2) Field-effect photodetectors have  $\sim\mu\text{m}$  scale channel length which requires highly focused laser beams as actuators and do not work well for weak infrared illumination; (3) Most current PTE photodetectors have a long lateral channel for effective heat dissipation and require localized illumination on p–n junctions or interfaces during photon detection.

In this work, we demonstrate a self-powered, large-area, compact, and broadband infrared photodetector as well as energy harvester by exploiting a vertical temperature gradient in a CNTF black-body absorber. Light reflection is significantly suppressed in the self-assembled CNTF due to sparseness and vertical alignment of nanotubes.<sup>19</sup> By employing this vertically aligned anti-reflecting nanowire array,<sup>14,17</sup> the macroscopic PTE photodetector has achieved high responsivity to an unfocused and broadband infrared light as low as 6.8  $\mu\text{W mm}^{-2}$ , akin to many realistic scenarios. We find the optimized PTE performance yielded in a top conductive layer having the appropriate thickness and a low contact resistance. A broadband responsivity of 5.3 V W<sup>-1</sup> in 2.5–25  $\mu\text{m}$  spectral range and peak responsivity of 640 V W<sup>-1</sup> at 4.3 THz are

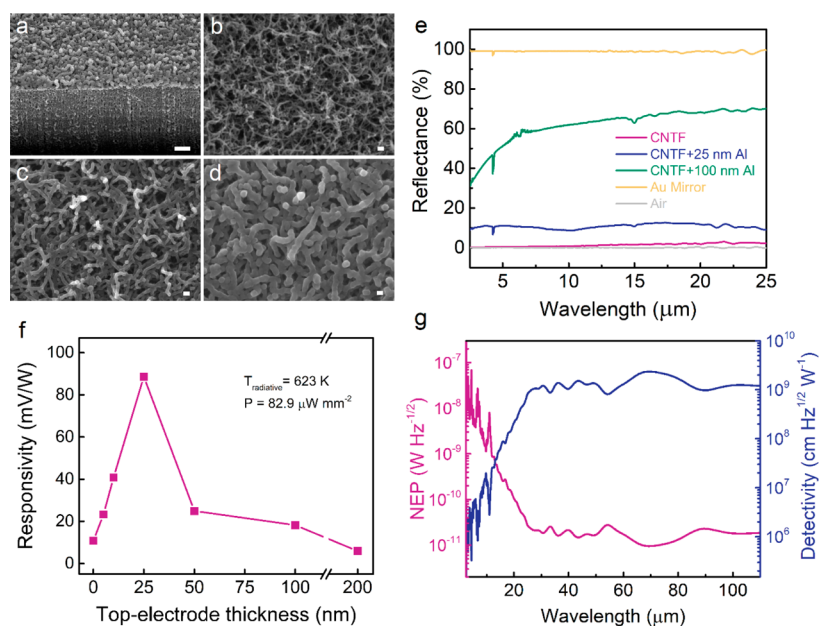


**Figure 2.** Morphology, infrared absorption, and photoresponse of metal covered CNTFs. (a) SEM morphology of a 200 nm Al/CNTF junction viewed at 35° tilted angle. The scale bar is 1 μm. (b–d) SEM morphologies of top-viewed 25, 50, and 100 nm Al covered CNTFs. The scale bar is 100 nm. (e) Infrared reflectance spectrum of air, pristine CNTF, 25 nm Al covered CNTF, 100 nm Al covered CNTF, and gold in 2.5–25 μm spectral range. The reflectance of air (0.03%) and gold mirror (99.0%) are listed for reference. (f) Photoresponsivity correlation with various Al thicknesses covered on CNTFs. The device photosensitive areas are 1 mm<sup>2</sup>. (g) Specific detectivity as a function of wavelength measured in a 25 nm Al covered CNTF device with 0.05 mm<sup>2</sup> area.

observed in this CNTF-based photodetector, yet with plenty of room for performance improvement.

## RESULTS AND DISCUSSION

**Photodetection Mechanism and Functionalities.** The photodetector schematic diagram is illustrated in Figure 1a. A densely packed CNTF grown by low-pressure chemical vapor deposition (LPCVD) is sandwiched by two electrodes on a Si substrate. The top-electrode layer connecting individually self-standing CNTs is deposited by magnetron sputtering. The photodetection mechanism is based on photothermoelectric effect: The cold p-type carriers at the bottom of CNTF diffuse toward the illuminated hot top side, as evidenced by zero-bias photocurrent direction shown in Figure 1a–c. Incident light waves are trapped and absorbed by the top-electrode/CNTF junction region, as the CNTF height (~100 μm) exceeds typical CNT perfect absorbers (~10 μm).<sup>20,21</sup> Then the top region of the device becomes thermalized due to electron excitation, while the bottom electrode and substrate serve as heat sink. The thermoelectric voltage output induced by the temperature gradient can be described by

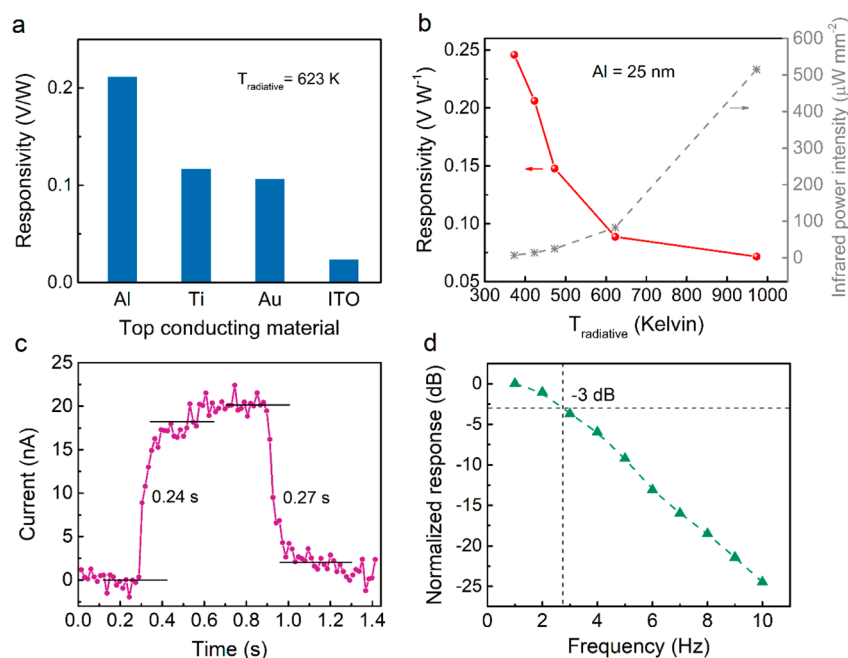
$$V = \int_{\text{bottom}}^{\text{top}} S(z) \nabla T(z) dz = \int S_{\text{Al}}(z) \nabla T_{\text{Al}}(z) dz + \int S_{\text{CNTs}}(z) \nabla T_{\text{CNTs}}(z) dz \quad (1)$$

Figure 1b indicates that under broadband radiation emitted from a black-body source, the device exhibits a subsecond temporal behavior of current in response to the light source switching on and off. Figure 1c presents the ohmic current–voltage characteristics of the photodetector in the dark and under illumination conditions, and a net photocurrent is observed at zero external bias. Under thermal radiation of 514.9 μW mm<sup>-2</sup> at 973 K source temperature, an open-circuit voltage of 44 μV and a short-circuit current 58 nA are

generated. This means the self-power merit of this PTE detector has demonstrated an additional functionality in energy harvesting, which may find applications in industrial waste-heat recycling and wearable human-body radiation collections.

**Morphology, Infrared Absorption, and Photoresponse.** The Raman spectrum (Figure S1) of an as-grown sample confirms the existence of CNTs and reveals the chirality information (Note S1), and the UV–vis spectrum (Figure S2) further indicates the material bandgap. The scanning electron microscope (SEM) morphologies of pristine and metal-covered CNTFs are presented in Figure S3a and Figure 2a–d. Figure 2a shows the intersection of the top surface and side wall of the CNTF/Al junction, and Figure 2b–d show the top-viewed CNTF morphologies with increasing Al coverage. It is clearly shown that as the metal coverage increases, the nanotube diameter grows larger which is roughly equal to the thickness of metal deposited (as shown in Figure S3b). The infrared reflectance curves measured by Fourier-transform infrared spectroscopy (FTIR) prove efficient light–matter interaction in CNTFs. For the 2.5–25 μm spectral range, optical reflectance of 0.57%, 10.4%, and 49.2% are observed in the pristine CNTF, 25 nm Al covered CNTF, and 100 nm Al covered CNTF, respectively, as shown in Figure 2e. Compared to horizontal CNT thin-film or bulk Al film, the significant suppressions of reflectance in pristine and metal covered CNTFs can be explained as (1) the homogeneous sparseness and vertical alignment of CNTs have induced refractive-index matching at air–CNTF interface; and (2) the slightly tilted CNT alignment allows photons bounce back and forth many times without escaping.<sup>19</sup> Overall, the lithography-free CNTF absorber provides an efficient light-absorbing platform for broadband infrared photodetection.

**PTE Engineering of CNTF Top Conductive Layer.** The primary task of constructing the vertical detector is to



**Figure 3.** PTE response correlation with top-electrode materials, illumination power and operating frequency. (a) Photoresponse of CNTF detectors covered by four kinds of conductive materials. The photoresponse of each junction is an averaged value by two devices. (b) Photoresponse (in red dots) of an Al covered CNTF detector under different radiative temperature, that is, different incident power density. The detector received illumination power intensities (the gray stars) are  $514.9 \mu\text{W mm}^{-2}$  (973 K),  $82.9 \mu\text{W mm}^{-2}$  (623 K),  $24.6 \mu\text{W mm}^{-2}$  (473 K),  $14.2 \mu\text{W mm}^{-2}$  (423 K), and  $6.8 \mu\text{W mm}^{-2}$  (373 K), respectively. (c) Detector rise and fall times characterized by a black-body radiation source at 973 K ( $\sim 350 \mu\text{W mm}^{-2}$ ). (d) Frequency response showing a 3 dB frequency at  $\sim 2.8$  Hz. The top-electrode thickness photosensitive area of above device is 25 nm and  $1 \text{ mm}^2$ , respectively.

effectively collect and convert the light-induced temperature gradient in CNTF into notable electric signals. When the top and bottom surfaces of a pristine CNTF are simply connected by a lead wire, the measured photoresponsivity  $R_V$  (defined as photovoltage divided by incident infrared power) is very low, only  $11 \text{ mV W}^{-1}$ . After the Al layer is deposited on three CNTFs with increasing thickness of 5 nm, 10 nm, and 25 nm, the photoresponsivity has seen an 8-fold rise to  $89 \text{ mV W}^{-1}$  in 25 nm Al covered CNTF, as shown in Figure 2f. We explain this phenomenon in two aspects. First, for the pristine CNTF device, as the vertical electrical conductivity of CNTF is much higher than the horizontal counterpart,<sup>28</sup> only a small portion of photocurrent right under silver paste can be collected because other individual CNTs are short-circuited. Thus, even though light absorption is maximized in pristine CNTF, its photoresponse is relatively low. Second, the presence of an Al layer on CNTF has constituted a junction which improves the Seebeck coefficient in the vicinity of the interface. This is attributed to the sharp inversion of carrier concentration from the hole-transporting CNTs to the electron-transporting metal.<sup>29</sup> The improvement of photoresponse as Al increases from 5 to 25 nm is found consistent to the behavior of Seebeck coefficient in nanoscale metal films (see Note S2).<sup>30</sup> However, when the Al layer deposited on CNTF becomes thicker, the photoresponsivity exhibits a decay due to significant infrared reflection which is the main limit of PTE response under this condition (the skin-depth of Al is 7.5–24 nm for 2.5–25  $\mu\text{m}$  spectral range).

To compare the performance of our device with other photodetectors, the noise equivalent power (NEP) and detectivity are utilized to evaluate the capability of identifying the weakest illumination from noise. The detector current

noise is characterized in Figure S4, where  $1/f$  noise, shot noise, and Johnson–Nyquist noise commonly contribute to the overall noise at low-frequency. But because the device operates at zero-bias condition,  $1/f$  noise and shot noise have been significantly suppressed (see Note S3).<sup>1,8,22,24,31,32</sup> The noise level quickly approaches a constant value starting from a relatively low frequency (around 3 dB corner frequency),<sup>5</sup> which is analogous to the noise shape measured in CNT PTE detector.<sup>24</sup> Figure S5 shows the zero-biased wavelength dependent photoresponsivity  $R_V$  ( $R_V = V/P$ ) of the CNTF detector (25 nm-thick Al,  $0.05 \text{ mm}^2$  device area) in the spectral range from 2.5 to  $110 \mu\text{m}$ . As the wavelength increases from 2.5 to  $25 \mu\text{m}$ , calculated  $R_V$  increases sharply from below  $1 \text{ V W}^{-1}$  to  $\sim 300 \text{ V W}^{-1}$  and then keeps relatively stable at several hundred  $\text{V W}^{-1}$  in the spectral range of 30– $110 \mu\text{m}$ . Since the detector noise level is independent of incident spectrum, the room-temperature NEP and detectivity as a function of wavelength are plotted in Figure 2g. NEP is calculated by  $i_n R/R_V$ , where  $R$  is the resistance and  $i_n$  is the measured current noise at 1 Hz. The specific detectivity  $D^*$  is extracted as  $D^* = (A\Delta f)^{1/2}/\text{NEP}$ , where  $\Delta f$  is integration time and  $A$  is photosensitive area. The  $D^*$  exhibits  $\sim 10^7$  to  $10^8 \text{ cm Hz}^{1/2} \text{ W}^{-1}$  in MWIR/LWIR regimes and  $\sim 10^8$  to  $10^9 \text{ cm Hz}^{1/2} \text{ W}^{-1}$  in FIR or THz regime. It is proposed that the elevated photoresponse in THz regime (peak at 4.3 THz) is due to the plasmon resonance enhanced light absorption and weak hot-carrier relaxation under low-energy photon excitation (discussed in Note S4). The detector performance rivals other PTE photodetectors as compared in Table S1.

Next, we alter the top-electrode layer by various conductive materials to investigate the change of PTE properties.<sup>22,24,33</sup> Four kinds of top-electrodes with equal thickness of 25 nm

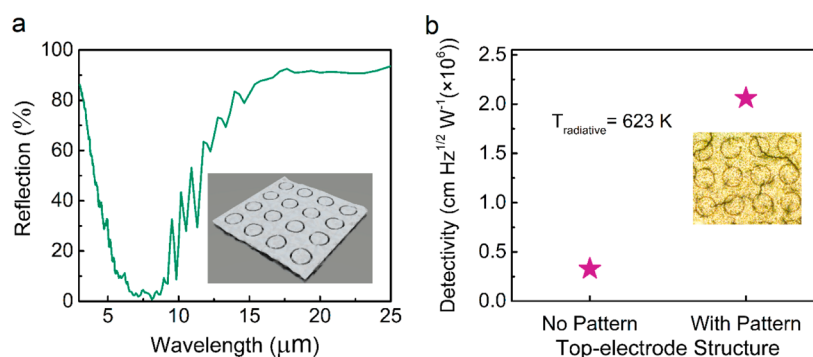


**Figure 4. Patterned top electrode.** (a) Simulated reflectance spectrum of a CNTF photodetector with periodic ring-shape patterns, showing a dip between 5 and 10  $\mu\text{m}$  wavelength. The inset shows the schematic of the patterns whose period, outer diameter, and inner diameter are 50  $\mu\text{m}$ , 38  $\mu\text{m}$ , and 32  $\mu\text{m}$ , respectively. (b) Photoresponse comparison of two CNTF photodetectors with and without periodic patterns in the 200 nm Al top-electrode. Inset: Optical image of the ring-shape patterned top-electrode.

form junctions with CNTF: CNTF/Al, CNTF/Ti, CNTF/Au, and CNTF/ITO. Figure 3a shows the different photoresponse in these junctions: the CNTF/Al junction performs the best followed by CNT/Ti, CNTF/Au, and CNTF/ITO. It has been recognized that the thermal and the electrical contact qualities of a junction have significant impacts on thermoelectric efficiency.<sup>34–36</sup> High thermal barrier resistance leads to reduced temperature gradient, and high electrical contact resistance leads to lower Seebeck coefficient in the vicinity of the interface.<sup>35,37</sup> Here, we speculate that different Seebeck coefficient offsets between top-electrode material and CNTF, and different junction induced thermal gradients (physical parameters of these four junctions are listed in Table S2) commonly contribute to the photoresponse results in Figure 3a. The low response of CNTF/Au and CNTF/ITO junctions is considered due to the poor thermal and electrical contacts from Au and ITO.

**Weak Illumination Sensitivity and Frequency Response.** The photoresponse correlation with illumination power-density is obtained by setting the temperature of the black-body source to 973 K, 623 K, 473 K, 423 K, and 373 K and measuring the photoresponse, respectively. When the radiative temperature decreases, the peak wavelength of radiative spectrum shifts from 3.0 to 7.8  $\mu\text{m}$ , and the power density received by the detector also decreases. The power density is calculated by geometrical sizes and distances using the black-body radiation spectrum shown in Figure S6. Table S3 indicates that the higher the illumination power, the higher the measured  $\Delta T$  between hot-side and cold-side, and so higher output voltages are expected. But the relation between photovoltage output and infrared power is found not linear. As the radiative temperature decreases from 973 K ( $514.9 \mu\text{W mm}^{-2}$ ) to 373 K ( $6.8 \mu\text{W mm}^{-2}$ ), the observed photoresponsivity sees an increase from  $0.07 \text{ V W}^{-1}$  to  $0.25 \text{ V W}^{-1}$ , as shown in Figure 3b, meaning an improved photoresponse at lower illumination power density. This nonlinearity mostly originates from the thermal saturation at higher infrared power density due to the less efficient cold-end (substrate) cooling (see Note S5). Under a quite low illumination of  $6.8 \mu\text{W mm}^{-2}$ , 1.5 nA photocurrent is measured under zero-bias condition. The high sensitivity at weak illumination power is considered to benefit from the extreme light absorption of CNTF and efficient thermoelectric conversion in the vertical metal/CNTF junction.<sup>17</sup> This feature could find practical significance in real-world photodetection since the infrared radiation to be detected/harvested is usually much weaker than

the laser output. Moreover, this architecture might contribute to establishing mid-infrared single-photon detection, in analogy to a vertical indium phosphide nanowire array used for room-temperature single-photon detection in the visible range.<sup>38</sup>

The detector response speed and frequency response are characterized in Figure 3c,d. Both measurements were carried out using a 973 K black-body radiation source with peak power at 3.0  $\mu\text{m}$ . Figure 3c shows the rise time (from 10% to 90% stable current) and decay time (from 90% to 10% stable current) of the detector response switching between dark and light conditions. A rise time of  $\tau_{\text{rise}} = 0.24 \text{ s}$  and a fall time of  $\tau_{\text{decay}} = 0.27 \text{ s}$  are obtained under  $\sim 350 \mu\text{W mm}^{-2}$  illumination, while a relatively faster response times of  $\tau_{\text{rise}} = \tau_{\text{decay}} = 0.17 \text{ s}$  are obtained under  $\sim 90 \mu\text{W mm}^{-2}$  (Figure S7a). The scale of response time is determined by the PTE effect mechanism which is typically slower than photovoltaic effects<sup>5,39</sup> and also related to the long channel ( $\sim 100 \mu\text{m}$ ) induced large heat capacity.<sup>8</sup> The slightly shorter response-time under low-power illumination is because the equilibrium of a small thermal gradient can be built up more rapidly. Figure S7b shows the detector time response under THz window filtered black-body radiation (cutoff frequency at 15 THz). Under longer wavelength excitation, a rise time of  $\tau_{\text{rise}} = 0.20 \text{ s}$  and a fall time of  $\tau_{\text{decay}} = 0.23 \text{ s}$  are obtained. Frequency response shown in Figure 3d presents that the 3 dB point occurs at  $\sim 2.8 \text{ Hz}$  under the black-body radiation.

**Patterning the Top Electrode.** As a pathway to improve light absorption in the presence of a top metallic layer, we design and fabricate microscale (Figure 4a inset) and nanoscale (Figure S8) periodic patterns in the top-electrode (Al) to mitigate reflection. The optical simulation is carried out by finite element method in COMSOL Multiphysics. Polarization-independent ring-shape patterns with 50  $\mu\text{m}$  period, 38  $\mu\text{m}$  outer diameter, and 32  $\mu\text{m}$  inner diameter are chosen to minimize incident infrared reflection due to impedance matching. A simulated reflection spectrum in Figure 4a shows that these patterns exhibit a reflection dip at around 4–12  $\mu\text{m}$  spectral range where most of the black-body radiation is situated. Here the light transmittance is treated as zero due to the presence of bottom metallic layers, and infrared absorption of the photodetector is  $A(\omega) = 1 - R(\omega) - T(\omega) = 1 - R(\omega)$ , where  $A$ ,  $R$ , and  $T$  are the absorption, reflectance, and transmittance, respectively. Figure 4b shows that the measured photodetectivity in 2.5–25  $\mu\text{m}$  range exhibits a 6-fold increase after patterning the Al layer deposited on CNTF,

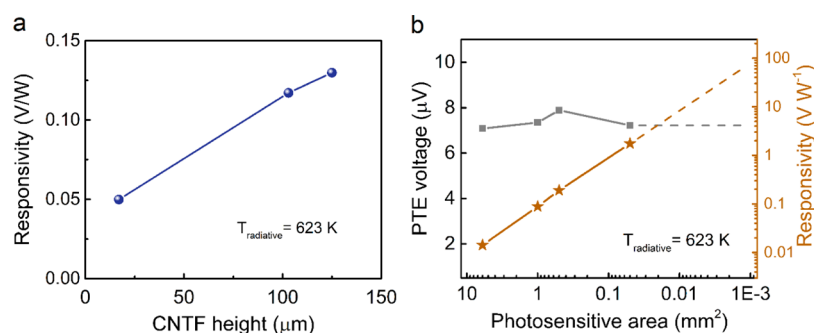


**Figure 5.** Photoresponsivity improvement by optimizing CNTF height and photosensitive area. (a) Detector responsivity improves with increasing CNTF height. The CNTF heights are 17  $\mu\text{m}$ , 103  $\mu\text{m}$ , and 125  $\mu\text{m}$ , respectively, determined by SEM. (b) The PTE voltage has seen small variation between 7.89  $\mu\text{V}$  and 7.08  $\mu\text{V}$  by decreasing the photosensitive area from 6  $\text{mm}^2$  to 0.05  $\text{mm}^2$ , and the calculated photoresponsivity increases by 123-fold to 1.7  $\text{V W}^{-1}$  correspondingly. Dash lines show the predicted PTE response for even smaller photosensitive areas.

demonstrating the capability to improve photoresponse by integrating patterned metallic layer on CNTF.

**Performance Optimization.** The best broadband photoresponsivity  $R_V$  and detectivity  $D^*$  are 5.3  $\text{V W}^{-1}$  and  $1.9 \times 10^7 \text{ cm Hz}^{1/2} \text{ W}^{-1}$  in 2.5–25  $\mu\text{m}$  spectral range, and the peak values achieve 640  $\text{V W}^{-1}$  and  $2.3 \times 10^9 \text{ cm Hz}^{1/2} \text{ W}^{-1}$  at 70  $\mu\text{m}$  wavelength (4.3 THz). The possibilities of performance optimization are shown in Figure 5 regarding CNTF height and area and discussed in Note S6 regarding CNT diameter, density, and mobility. Enhanced PTE response is observed in CNTF with extended height as shown in Figure 5a, because the longer channel is expected to sustain elevated temperature gradient.<sup>25,40</sup> The photoresponse is estimated to increase nearly an order of magnitude if the CNTF could achieve  $\sim\text{mm}$  height as in ref 41, which is the typical size of a thermoelectric component. Figure 5b shows the correlation between measured and predicted photoresponsivity  $R_V$  with decreasing photosensitive area  $A$  (the lateral size of CNTF) in 2.5–25  $\mu\text{m}$ . It is found that as  $A$  decreases from 6  $\text{mm}^2$  to 0.05  $\text{mm}^2$ , the photovoltage only sees a slight variation within 7.08  $\mu\text{V}$  to 7.89  $\mu\text{V}$ , but the  $R_V$  increases dramatically from 14  $\text{mV W}^{-1}$  to 1.7  $\text{V W}^{-1}$  as calculated by

$$R_V = \frac{V}{P} = \frac{\int_{\text{bottom}}^{\text{top}} S(z) \nabla T(z) dz}{A \times p_{\text{uniform}}} \quad (2)$$

where  $A$  is the photosensitive area and  $p_{\text{uniform}}$  is the incident power density. The reason for the constant photovoltage under various photosensitive areas is that PTE voltage is determined by thermal gradient in  $z$  direction instead of  $x$ – $y$  plane in this 3D architecture as illustrated by eq 1 and Figure S9. Considering the photosensitive area in this work is much larger than most state-of-the-art (Table S1), the photoresponsivity is predicted to further increase in even smaller size devices,<sup>8</sup> although some reasons may lead to a final degradation.

For a broader interest, this photodetector architecture is applicable to other nanowire arrays (e.g., semiconducting nanowires with higher Seebeck coefficients), and top conductive layer (e.g.,  $\text{MoS}_2$ , black phosphorus) combinations providing a high-quality contact is formed. Advantages of this vertical PTE junction architecture are three-fold. First, compared to a planar–interface PTE detector, the photoresponse in a vertical photojunction is relatively insensitive to illumination spot position, mitigating the optical alignment and

focusing requirements. Second, the device compactness is less likely to be compromised when the PTE channel can be extended in vertical direction for heat dissipation, facilitating the integration of a compact detector array. Third, for energy harvesting purposes, the ease of expanding the light-harvesting area brings convenience to large-area integration.

## CONCLUSIONS

In summary, we demonstrate a self-powered, large-area, and broadband infrared photodetector by employing vertical PTE effect of high-density CNTF with nearly unity black-body absorption properties. A broadband photodetectivity of  $1.9 \times 10^7 \text{ cm Hz}^{1/2}$  in 2.5–25  $\mu\text{m}$  spectral range and a peak detectivity of  $2.3 \times 10^9 \text{ cm Hz}^{1/2}$  at 4.3 THz are achieved under weak, unfocused, and broadband infrared illumination akin to realistic scenarios. The photodetectors are implemented through PTE engineering of the top-electrode layer. The material, thickness, and pattern are investigated regarding the photoresponse, whose further improvement is also indicated by increasing the height or decreasing the lateral size of CNTF. The exemplified device might find applications in room-temperature, self-powered, and broadband infrared detection or energy harvesting for real-time health condition monitoring, low-cost industrial inspection, and distributed sensing/power supplying in the Internet of Things.

## METHODS

**Growth of CNT Forest.** Vertically aligned CNTFs were grown by low-pressure chemical vapor deposition (LPCVD) at 660  $^\circ\text{C}$  and 15 mbar in an Aixtron Black Magic 2 system with  $\text{C}_2\text{H}_2$  as carbon source. Prior to CNT growth, 20 nm Ti bottom electrode, 10 nm Al catalyst diffusion barrier, and 0.8 nm Fe catalyst film were deposited by magnetron sputtering (AJA Orion twin chamber) onto doped Si substrates previously back-side metallized with Ti/Au using e-beam evaporation. For a typical 30 min growth, the CNTF height is  $\sim 100 \mu\text{m}$ .

**Device Fabrication.** Four kinds of top-electrode materials: Al, Ti, Au, and ITO are deposited on CNTF all by magnetron sputtering due to the conformal step-coverage around CNTs tips and better electrical contact compared to evaporation. The 3  $\mu\text{m}$  feature-size and 130 nm feature-size periodic patterns in Al top-electrodes were etched by inductively coupled plasma-reactive ions etching (Oxford Plasma lab). Etching masks were patterned by UV lithography (Suss MA6Mask Aligner) with S1811 as positive-tone photoresist and by electron beam lithography (RAITH150-TWO) with ZEP-520A as positive-tone e-beam resist, respectively. Finally, the device is glued to the

cathode on a chip carrier, and a thin gold-wire connected to anode pin is then glued onto CNTF top-electrode by silver conductive epoxy.

**Material Characterizations.** Scanning electron microscopy (SEM) images of CNTF and Al covered CNTF were taken in a JEOL JSM 7200F field emission SEM at 5 kV/10 kV voltage with 8–10 nA beam current. The Raman spectrum of CNTF was obtained in Bruker Senterra-2 Raman spectrometer under 532 nm light excitation. The UV–vis spectrum was measured in a PerkinElmer Lambda 35 and 1050 UV–vis spectrometer. The infrared reflectance is characterized by FTIR spectrometer (Nicolet iS50R FT-IR Thermo Scientific).

**Device Measurement.** A broadband, unfocused black-body radiation source (Newport Oriel 67030) was used to imitate real-world mid-infrared emission when measuring the detector photo-response. The black-body temperature is set from 373 to 973 K with an opening spot diameter varying from 0.1 in. to 1 in., and photodetectors to be measured are placed 25 mm away.  $I$ – $V$  characteristics and currents with and without black-body illumination were measured by a Keithley 6487 pico-ammeter. The photothermoelectric voltages at zero-bias were calculated from measured photocurrents by  $V = IR$ , where  $R$  represents resistance of the device. The broadband spectral response was characterized by a FTIR spectrometer (Nitrogen gas purged IFS50, Thermo Scientific) where the detector was excited by two light sources (Globar, 2.5–25  $\mu\text{m}$  and 16.7–200  $\mu\text{m}$ ) calibrated by a deuterated triglycine sulfate detector with or without polyethylene filter. The resulting photoresponse was directly measured by the FTIR internal ammeter without amplifying. For frequency response measurement, the output beam of black-body was modulated by an optical chopper before shining onto the detector, and the output electric signal from the detector was fed into an SR830 lock-in amplifier with a reference frequency related to the optical chopper. Current noise spectrum was measured using a 4200A-SCS parameter analyzer in an isolated metal-box at ambient condition.

**Optical Simulation.** The detector is simulated by finite element method using COMSOL Multiphysics 5.0, RF module. Periodic boundary conditions were established in  $x$  and  $y$  directions, and a perfectly matched layer was placed in  $z$  direction above detector surface. The top (200 nm Al) and bottom (10 nm Al and 20 nm Ti) layers were treated as perfect electric conductor layers, and the electrical conductivity of CNTF was modeled as (1, 1, 300) S/m<sup>28</sup> along the  $x$ – $y$ – $z$  axis. The top metallic layer pattern consists of 50  $\mu\text{m}$  period, ring-shaped patterns with 19 and 16  $\mu\text{m}$  outer and inner radius, respectively. The light wave in a frequency range of 10–100 THz (3–30  $\mu\text{m}$ ) is normally incident onto the detector surface.

## ASSOCIATED CONTENT

### Supporting Information

The Supporting Information is available free of charge on the ACS Publications website at DOI: 10.1021/acsnano.9b06332.

Raman, UV–vis, and SEM characterizations of pristine and Al covered CNTFs, current noise spectrum, photoresponsivity as a function of wavelength, profiles of black-body spectral radiant emittances at various temperatures, rise/decay time response of detector, measurement of CNTF with electron-beam lithography patterned Al top-electrode, drawing of photodetector equivalent circuit, a list of physical properties for four top-electrode/CNTF junctions, measured and calculated device temperature under global infrared illumination, comparison between this work and representative PTE photodetectors, chirality of CNTF, Seebeck coefficient of metal thin-film, detector noise, elevated photo-response at THz range, device temperature gradient, CNT diameter, density, and mobility influence on PTE effect (PDF)

## AUTHOR INFORMATION

### Corresponding Author

\*E-mail: jyeow@uwaterloo.ca.

### ORCID

Mingyu Zhang: 0000-0003-3531-7369

Dayan Ban: 0000-0002-5271-3163

Chao Xu: 0000-0002-1671-7888

John T. W. Yeow: 0000-0002-0740-8055

### Notes

The authors declare no competing financial interest.

## ACKNOWLEDGMENTS

This work is supported by the Natural Sciences and Engineering Research Council of Canada (NSERC), Canada Research Chairs program (CRC) to J.Y. and CMC Microsystems Micro-Nano Technology (MNT) Financial Assistance (project reference ID: 5487). The authors acknowledge Chen Chen, Zhou Zheng, and Yue Zhuo for some material characterizations and Dr. Fred Sun and Dr. Yunhan Li for helpful discussions.

## REFERENCES

- (1) Bullock, J.; Amani, M.; Cho, J.; Chen, Y.; Ahn, G. H.; Adinolfi, V.; Shrestha, V. R.; Gao, Y.; Crozier, K. B.; Chueh, Y.; Javey, A. Polarization-Resolved Black Phosphorus/Molybdenum Disulfide Mid-Wave Infrared Photodiodes with High Detectivity at Room Temperature. *Nat. Photonics* **2018**, *12*, 601–607.
- (2) Zhang, M.; Yeow, J. Nanotechnology-Based Terahertz Biological Sensing. *IEEE Nanotechnol. Mag.* **2016**, *10*, 30–38.
- (3) Tonouchi, M. Cutting-Edge Terahertz Technology. *Nat. Photonics* **2007**, *1*, 97–105.
- (4) Chen, X.; Lu, X.; Deng, B.; Sinai, O.; Shao, Y.; Li, C.; Yuan, S.; Tran, V.; Watanabe, K.; Taniguchi, T.; Naveh, D.; Yang, L.; Xia, F. Widely Tunable Black Phosphorus Mid-Infrared Photodetector. *Nat. Commun.* **2017**, *8*, 1672–1678.
- (5) Long, M.; Gao, A.; Wang, P.; Xia, H.; Ott, C.; Pan, C.; Fu, Y.; Liu, E.; Chen, X.; Lu, W.; Nilges, T.; Xu, J.; Wang, X.; Hu, W.; Miao, F. Room Temperature High-Detectivity Mid-Infrared Photodetectors Based on Black Arsenic Phosphorus. *Sci. Adv.* **2017**, *3*, e1700589.
- (6) Low, T.; Avouris, P. Graphene Plasmonics for Terahertz to Mid-Infrared Applications. *ACS Nano* **2014**, *8*, 1086–1101.
- (7) Sassi, U.; Parret, R.; Nanot, S.; Bruna, M.; Borini, S.; Milana, S.; De Fazio, D.; Zhao, Z.; Lidorikis, E.; Koppens, F. H. L.; Ferrari, A. C.; Colli, A. Graphene-Based, Mid-Infrared, Room-Temperature Pyroelectric Bolometers with Ultrahigh Temperature Coefficient of Resistance. *Nat. Commun.* **2017**, *8*, 1433.
- (8) Mauser, K. W.; Kim, S.; Mitrovic, S.; Fleischman, D.; Pala, R.; Schwab, K. C.; Atwater, H. A. Resonant Thermoelectric Nanophotonics. *Nat. Nanotechnol.* **2017**, *12*, 770–775.
- (9) Shautsova, V.; Sidiropoulos, T.; Xiao, X.; Guskens, N. A.; Black, N. C. G.; Gilbertson, A. M.; Giannini, V.; Maier, S. A.; Cohen, L. F.; Oulton, R. F. Plasmon Induced Thermoelectric Effect in Graphene. *Nat. Commun.* **2018**, *9*, 5190.
- (10) Yu, X.; Dong, Z.; Yang, J. K. W.; Wang, Q. J. Room-Temperature Mid-Infrared Photodetector in All-Carbon Graphene Nanoribbon-C60 Hybrid Nanostructure. *Optica* **2016**, *3*, 979–984.
- (11) Cai, X.; Sushkov, A. B.; Jadidi, M. M.; Nyakiti, L. O.; Myers-Ward, R. L.; Gaskill, D. K.; Murphy, T. E.; Fuhrer, M. S.; Drew, H. D. Plasmon-Enhanced Terahertz Photodetection in Graphene. *Nano Lett.* **2015**, *15*, 4295–4302.
- (12) Tang, X.; Ackerman, M. M.; Guyot-Sionnest, P. Thermal Imaging with Plasmon Resonance Enhanced HgTe Colloidal Quantum Dot Photovoltaic Devices. *ACS Nano* **2018**, *12*, 7362–7370.

- (13) Chou, L. W.; Shin, N.; Sivaram, S. V.; Filler, M. A. Tunable Mid-Infrared Localized Surface Plasmon Resonances in Silicon Nanowires. *J. Am. Chem. Soc.* **2012**, *134*, 16155–16158.
- (14) Cao, Y.; Zhu, J.; Xu, J.; He, J.; Sun, J. L.; Wang, Y.; Zhao, Z. Ultra-Broadband Photodetector for the Visible to Terahertz Range by Self-Assembling Reduced Graphene Oxide-Silicon Nanowire Array Heterojunctions. *Small* **2014**, *10*, 2345–2351.
- (15) Jean, J.; Chang, S.; Brown, P. R.; Cheng, J. J.; Rekemeyer, P. H.; Bawendi, M. G.; Gradečak, S.; Bulovič, V. ZnO Nanowire Arrays for Enhanced Photocurrent in PbS Quantum Dot Solar Cells. *Adv. Mater.* **2013**, *25*, 2790–2796.
- (16) Tang, Y. B.; Chen, Z. H.; Song, H. S.; Lee, C. S.; Cong, H. T.; Cheng, H. M.; Zhang, W. J.; Bello, I.; Lee, S. T. Vertically Aligned p-Type Single-Crystalline GaN Nanorod Arrays on n-Type Si for Heterojunction. *Nano Lett.* **2008**, *8*, 4191–4195.
- (17) Walia, J.; Dhindsa, N.; Flannery, J.; Khodabad, I.; Forrest, J.; Lapierre, R.; Saini, S. S. Enhanced Photothermal Conversion in Vertically Oriented Gallium Arsenide Nanowire Arrays. *Nano Lett.* **2014**, *14*, 5820–5826.
- (18) Svensson, J.; Anttu, N.; Vainorius, N.; Borg, B. M.; Wernersson, L. E. Diameter-Dependent Photocurrent in InAsSb Nanowire Infrared Photodetectors. *Nano Lett.* **2013**, *13*, 1380–1385.
- (19) Mizuno, K.; Ishii, J.; Kishida, H.; Hayamizu, Y.; Yasuda, S.; Futaba, D. N.; Yumura, M.; Hata, K. A Black Body Absorber from Vertically Aligned Single-Walled Carbon Nanotubes. *Proc. Natl. Acad. Sci. U. S. A.* **2009**, *106*, 6044–6047.
- (20) Selvakumar, N.; Krupanidhi, S. B.; Barshilia, H. C. Carbon Nanotube-Based Tandem Absorber with Tunable Spectral Selectivity: Transition from Near-Perfect Blackbody Absorber to Solar Selective Absorber. *Adv. Mater.* **2014**, *26*, 2552–2557.
- (21) Yang, Z.; Ci, L.; Bur, J. A.; Lin, S.; Ajayan, P. M. Experimental Observation of an Extremely Dark Material Made By a Low-Density Nanotube Array. *Nano Lett.* **2008**, *8*, 446–451.
- (22) Cai, X.; Sushkov, A. B.; Suess, R. J.; Jadidi, M. M.; Jenkins, G. S.; Nyakiti, L. O.; Myers-Ward, R. L.; Li, S.; Yan, J.; Gaskill, D. K.; Murphy, T. E.; Drew, H. D.; Fuhrer, M. S. Sensitive Room-Temperature Terahertz Detection via the Photothermoelectric Effect in Graphene. *Nat. Nanotechnol.* **2014**, *9*, 814–819.
- (23) Erikson, K. J.; He, X.; Talin, A. A.; Mills, B.; Hauge, R. H.; Iguchi, T.; Fujimura, N.; Kawano, Y.; Kono, J.; Léonard, F. Figure of Merit for Carbon Nanotube Photothermoelectric Detectors. *ACS Nano* **2015**, *9*, 11618–11627.
- (24) Suzuki, D.; Oda, S.; Kawano, Y. A Flexible and Wearable Terahertz Scanner. *Nat. Photonics* **2016**, *10*, 809–813.
- (25) Zhang, M.; Yeow, J. T. W. Flexible Polymer - Carbon Nanotube Composite with High Response Stability for Wearable Thermal Imaging. *ACS Appl. Mater. Interfaces* **2018**, *10*, 26604–26609.
- (26) Viti, L.; Hu, J.; Coquillat, D.; Knap, W.; Tredicucci, A.; Politano, A.; Vitiello, M. S. Black Phosphorus Terahertz Photodetectors. *Adv. Mater.* **2015**, *27*, 5567.
- (27) Dresselhaus, M. S.; Chen, G.; Tang, M. Y.; Yang, R.; Lee, H.; Wang, D.; Ren, Z.; Fleurial, J. P.; Gogna, P. New Directions for Low-Dimensional Thermoelectric Materials. *Adv. Mater.* **2007**, *19*, 1043–1053.
- (28) Haddadi, K.; Tripon-Canselier, C.; Hivin, Q.; Ducournau, G.; Teo, E.; Coquet, P.; Tay, B. K.; Lepilliet, S.; Avramovic, V.; Chazelas, J.; Decoster, D. Microwave and Millimeter Wave Properties of Vertically-Aligned Single Wall Carbon Nanotubes Films. *J. Electron. Mater.* **2016**, *45*, 2433–2441.
- (29) Lyeo, H.; Lyeo, H.; Khajetoorians, A. A.; Shi, L.; Pipe, K. P. Profiling the Thermoelectric Power of Semiconductor Junctions with Nanometer Resolution. *Science* **2004**, *303*, 816–818.
- (30) Zhang, X.; Choi, H.; Datta, A.; Li, X. Design, Fabrication and Characterization of Metal Embedded Thin Film Thermocouples with Various Film Thicknesses and Junction Sizes. *J. Micromech. Microeng.* **2006**, *16*, 900–905.
- (31) Hesler, J. L.; Crowe, T. W.; Diodes, V. Responsivity and Noise Measurements of Zero-Bias Schottky Diode Detectors. Proceedings from the 18th International Symposium on Space Terahertz Technology 2007, Pasadena, California, March 21–23, 2007; Curran Associates, Inc.: Red Hook, NY, 2007; p 89.
- (32) Hsu, A. L.; Herring, P. K.; Gabor, N. M.; Ha, S.; Shin, Y. C.; Song, Y.; Chin, M.; Dubey, M.; Chandrakasan, A. P.; Kong, J.; Jarillo-Herrero, P.; Palacios, T. Graphene-Based Thermopile for Thermal Imaging Applications. *Nano Lett.* **2015**, *15*, 7211–7216.
- (33) Nanot, S.; Cummings, A. W.; Pint, C. L.; Ikeuchi, A.; Akiho, T.; Sueoka, K.; Hauge, R. H.; Léonard, F.; Kono, J. Broadband, Polarization-Sensitive Photodetector Based on Optically-Thick Films of Macroscopically Long, Dense, and Aligned Carbon Nanotubes. *Sci. Rep.* **2013**, *3*, 1335.
- (34) Sungtaek Ju, Y.; Ghoshal, U. Study of Interface Effects in Thermoelectric Microrefrigerators. *J. Appl. Phys.* **2000**, *88*, 4135.
- (35) da Silva, L. W.; Kaviany, M. Micro-Thermoelectric Cooler: Interfacial Effects on Thermal and Electrical Transport. *Int. J. Heat Mass Transfer* **2004**, *47*, 2417–2435.
- (36) Hao, F.; Fang, D. N.; Li, J. Y. Thermoelectric Transport in Heterogeneous Medium: The Role of Thermal Boundary Resistance. *Eur. Phys. J.: Appl. Phys.* **2012**, *58*, 30901.
- (37) Wang, S.; Xie, T.; Xie, H. Experimental Study of the Effects of the Thermal Contact Resistance on the Performance of Thermoelectric Generator. *Appl. Therm. Eng.* **2018**, *130*, 847–853.
- (38) Gibson, S. J.; van Kasteren, B.; Tekcan, B.; Cui, Y.; van Dam, D.; Haverkort, J. E. M.; Bakkers, E. P. A. M.; Reimer, M. E. Tapered InP Nanowire Arrays for Efficient Broadband High-Speed Single-Photon Detection. *Nat. Nanotechnol.* **2019**, *14*, 473–479.
- (39) Long, M.; Wang, Y.; Wang, P.; Zhou, X.; Xia, H.; Luo, C.; Huang, S.; Zhang, G.; Yan, H.; Fan, Z.; Wu, X.; Chen, X.; Lu, W.; Hu, W. Palladium Diselenide Long-Wavelength Infrared Photodetector with High Sensitivity and Stability. *ACS Nano* **2019**, *13*, 2511–2519.
- (40) Deng, X.; Wang, Y.; Zhao, Z.; Chen, Z.; Sun, J.-L. Terahertz-Induced Photothermoelectric Response in Graphene-Metal Contact Structures. *J. Phys. D: Appl. Phys.* **2016**, *49*, 425101.
- (41) Hata, K.; Futaba, D. N.; Mizuno, K.; Namai, T. Water-Assisted Highly Efficient Synthesis of Impurity-Free Single-Walled Carbon Nanotubes. *Science* **2004**, *306*, 1362–1365.